




## Article

# Study of the Kinetics of Reduction of IrO<sub>2</sub> on TiO<sub>2</sub> (Anatase) by Temperature-Programmed Reduction

Shahad Batubara <sup>1</sup>, Mogbel Alrushaid <sup>1</sup>, Muhammad Amtiaz Nadeem <sup>1</sup> and Hicham Idriss <sup>2,3,\*</sup><sup>1</sup> SABIC Technology Center (STC), King Abdullah University for Science and Technology (KAUST), Thuwal 23955, Saudi Arabia<sup>2</sup> Institute of Functional Interfaces (IFG), Karlsruhe Institute of Technology (KIT), 76131 Karlsruhe, Germany<sup>3</sup> Joint Research Center (JRC) of the European Union (EU), 76131 Karlsruhe, Germany

\* Correspondence: hicham.idriss@kit.edu

**Abstract:** The interaction between IrO<sub>2</sub> and TiO<sub>2</sub> (anatase) in non-isothermal reduction conditions has been studied by the temperature programmed reduction technique. IrO<sub>2</sub> clusters are of sizes between 0.5 and 0.9 nm as determined from High Resolution Transmission Electron Microscopy (HRTEM). Largely, two main regions for reduction were found and modeled at ca. 100 and 230 °C. The first region is attributed to the partial reduction of IrO<sub>2</sub> clusters, while the second one is due to reduction of the formed crystalline (rutile IrO<sub>2</sub>), during TPR, to Ir metal. Two methods for calculating kinetic parameters were tested. First, by applying different ramping rates on a 3.5 wt.% IrO<sub>2</sub>/TiO<sub>2</sub> using Kissinger's method. The apparent activation energy values for the first and second reduction regions were found to be ca. 35 and 100 kJ/mol, respectively. The second method was based on fitting different kinetic models for the experimental results in order to extract qualitative information on the nature of interaction during the reduction process. It was found that the first reduction is largely due to the amount of IrO<sub>2</sub> (reactant concentration) while the second one involved phase boundary effect as well as nucleation.

**Keywords:** IrO<sub>2</sub>/TiO<sub>2</sub> (anatase); temperature programmed reduction (TPR); IrO<sub>2</sub> cluster size; phase boundary effect; nucleation; activation energy



**Citation:** Batubara, S.; Alrushaid, M.; Amtiaz Nadeem, M.; Idriss, H. Study of the Kinetics of Reduction of IrO<sub>2</sub> on TiO<sub>2</sub> (Anatase) by Temperature-Programmed Reduction. *Inorganics* **2023**, *11*, 66. <https://doi.org/10.3390/inorganics11020066>

Academic Editors: Tzia Ming Onn and Raymond J. Gorte

Received: 23 December 2022

Revised: 11 January 2023

Accepted: 19 January 2023

Published: 31 January 2023



**Copyright:** © 2023 by the authors. Licensee MDPI, Basel, Switzerland. This article is an open access article distributed under the terms and conditions of the Creative Commons Attribution (CC BY) license (<https://creativecommons.org/licenses/by/4.0/>).

## 1. Introduction

Studying the nature of interaction between noble metals and the support on which they are dispersed is important for the design of catalytic materials [1]. Noble metals are deposited from their precursors, usually a salt, transformed to metal oxide clusters upon heating, then often reduced either prior or during a catalytic reaction. In order to obtain optimal dispersion on the support, and in some cases specific shape or a metallic cluster size [2], one needs to understand the interplay between the reduction process leading to these metal particles and the sintering process during which oxide clusters (and newly formed metal clusters) diffuse to larger ones. One of the kinetic methods that can shed light on this, and has been studied extensively, is temperature programmed reduction (TPR) [3,4]. These types of studies provide insights into how to optimize the catalyst's performance by understanding the extent of dispersion and regions where metal support interaction [5] occurs. In H<sub>2</sub>-TPR experiments the reduction of dispersed metal oxides is used to quantify H<sub>2</sub> consumption during a linearly increased temperature of the sample as a function of time under constant gas flow. The general reduction reaction is described as follows:



where M<sub>x</sub>O<sub>y</sub> is a metal oxide, and *x* and *y* are stoichiometric coefficients.

While TPR is a routine method for the characterization of dispersed metals, often over oxide supports, they are merely used as a diagnostic tool [6,7] and, in some cases,

to extract quantitative information (titration) needed to normalize reaction rates [8–10]. In catalytic studies, TPR is however seldomly used to model the kinetic of reduction of these metal oxide clusters (nano particles) to extract information related to their possible interaction with the surface of the support, during the reduction process. On the other hand, in materials science related research TPR is often used to study phase changes, growth, nucleation, diffusion, and related kinetics, all led to the development of different models over the years [11–14]. In general, two temperature domains exist during TPR, one at a low temperature (up to 250–300 °C) mostly due to the reduction of dispersed metal oxide clusters/particles to metals [15] and the other above that, and can have a contribution from the reduction of the support (in the case of reducible oxides) such as TiO<sub>2</sub>, CeO<sub>2</sub>, and Fe<sub>2</sub>O<sub>3</sub>, among others [16–18]. The majority of TPR studies are conducted for more commonly used noble metals such as Pt, Pd and Rh while Ir has received less attention. The fact that Ir is the most resistant known metal to corrosion and insoluble in mineral acids, makes it an important electrocatalyst that lies at the top of the volcano curve for oxygen anion oxidation, and is therefore among the most suitable elements for water splitting [19,20]. Its very high melting point [21] and its tendency of being well dispersed on supports, is also behind its thermal catalytic activity such as selective oxidation reactions, ethanol steam reforming to hydrogen and alkanes dehydrogenation [22–24]. Studying the properties of IrO<sub>2</sub> reduction to Ir would therefore provide further insights into its catalytic activity, in particular when affected by the support, which in turn controls the particle's size, shape, and composition [25,26]. One of the often common questions regarding a TPR profile is the origin of multiple peaks during ramping. Both their number which can be two, three or even more and their shape have been found to give indication on the reduction mechanism. For example, when two peaks occur in the region where noble metals are reduced one may invoke a step wise reduction ( $M^{x+}$  to  $M^{y+}$  to  $M^0$ ; where  $y < x$ ) or a change in the clusters' configuration (such as during sintering).

In a previous work we have studied the catalytic activity of IrO<sub>2</sub>/TiO<sub>2</sub> (anatase) for water oxidation in the presence of Ce<sup>4+</sup> cations (as electron scavengers) [27]. In this previous work, the % of Ir was studied for a wide range, from 0.1 to 4 wt.%. X-ray photoelectron spectroscopy (XPS) Ir4f showed that “as prepared” catalysts are exclusively composed of Ir<sup>4+</sup>, while XRD showed that only above 400 °C where weak diffraction lines due to the rutile IrO<sub>2</sub> can be detected. High-Resolution Transmission Electron Spectroscopy (HRTEM) and TEM images showed that the mean particle size changed from about 0.5 nm for 0.3 wt.% IrO<sub>2</sub> to about 0.9 nm for 4 wt.% IrO<sub>2</sub> on TiO<sub>2</sub> (anatase), and the dispersion changed from ca. 100% for 0.1–0.3 wt.% Ir to ca. 50% for 3.5–4.0 wt.% Ir. The TPR shape was, however, found to be complex. This complexity has motivated us further to study the dynamic of its reduction to metal. In previous studies we have used model-free methods to analyze desorption profiles of products during Temperature Programmed Desorption (TPD) [28–32] and model-based methods [33] to study the mixed oxides reduction in isothermal condition. In this work, the TPR patterns of 3.5 wt.% IrO<sub>2</sub>/TiO<sub>2</sub> are presented, analyzed, and modeled. To conduct this, we have opted to compare one model-free method to a few model-based methods, as outlined in the experimental section. The choice of this catalyst is dictated by its tested high performance while its relatively high metal content would decrease the unavoidable analytical errors while conducting the study. The main objective of this present study is to obtain the rates of reductions that best defines the chemical processes occurring at the interface with TiO<sub>2</sub> (anatase).

## 2. Results and Discussion

TPR experimental results of the complete series of IrO<sub>2</sub>/TiO<sub>2</sub> catalysts from 0.1 to 4 wt.% were presented previously [27]. At high loading (at and above 1.5 wt.%), two regions are seen, with maximum reduction temperatures at around 100 and 250 °C, in addition to a third small peak at about 350 °C (ramping rates  $\beta = 10$  °C/min). The first one is exclusively due to IrO<sub>2</sub> reduction, whereas the second and third regions might be influenced by the support of TiO<sub>2</sub> (in part due to the spillover effect [34]) and possible strong metal support

interactions (SMSI) between the Ir clusters and the TiO<sub>2</sub> support [35–38]. Furthermore, TPR experiments conducted on two samples of a crystalline rutile and amorphous iridium oxides found that the amorphous iridium oxide is reduced at about 80 °C, while the rutile-phase iridium oxide is reduced at about 230 °C [39]. Therefore, it was concluded that the reduction temperature at around 90–100 °C is due to amorphous IrO<sub>2</sub> reduction, and the reduction at ca. 230 °C is largely due to rutile IrO<sub>2</sub> on TiO<sub>2</sub> anatase formed during the ramping.

Table 1 and Figure 1 present the reduction temperature, nominal amounts of iridium used, total hydrogen consumption, and the H/Ir values of each IrO<sub>2</sub>/TiO<sub>2</sub> catalyst. By only accounting for the first and the second peaks at 90 and 230 °C in calculating the number of moles of H and Ir (see Figure 2), the H/Ir stoichiometry was found to be close to 4. Irrespective, there is a linear increase in the total hydrogen consumption with increasing IrO<sub>2</sub> loading from 0.1 to 3.5 wt.% as seen in Figure 1.

**Table 1.** Extracted quantitative data from TPR of the series of IrO<sub>2</sub>/TiO<sub>2</sub> (anatase, BET surface area = 55 m<sup>2</sup>/g) catalysts as a function of IrO<sub>2</sub> content with a ramping rate  $\beta = 10$  °C/min.

Ir wt.% Loading ±0.01	Temperature Range °C ±1	Integrated Peak Area (cm <sup>3</sup> /g) ±0.1	IrO <sub>2</sub> (μmol/g)	Total H <sub>2</sub> Consumption (μmol/g) ±5%	H/Ir ±0.2
0.1	86–156	0.24	0.270	0.62	4.7
0.3	82–142	0.53	0.781	1.37	3.5
0.5	50–179	0.83	1.32	2.17	3.3
1.0	28–200	1.9	2.68	5.02	3.7
1.5	82–140	2.51	4.10	6.78	3.3
2.0	76–252	4.01	5.55	11.0	4.0
2.5	76–261	4.57	6.88	12.4	3.6
3.0	47–243	4.46	8.47	13.6	3.2
3.5	81–261	6.94	9.85	19.2	3.9

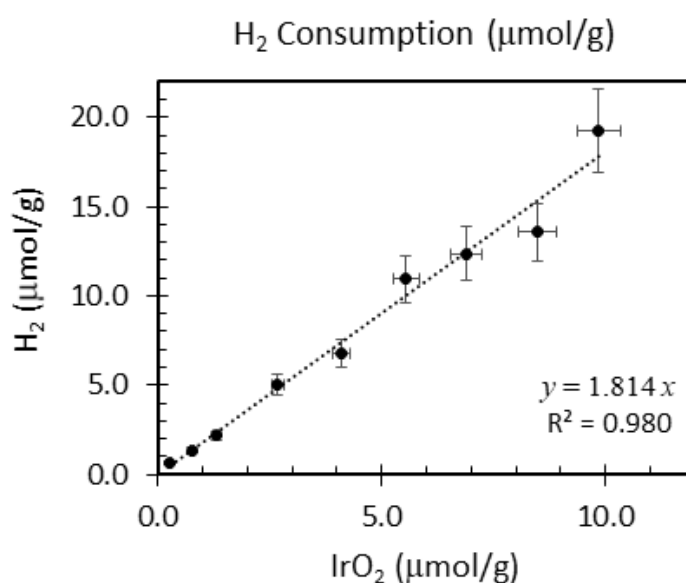


**Figure 1.** Normalized molecular hydrogen consumption per g of catalyst as a function of IrO<sub>2</sub> content for the IrO<sub>2</sub>/TiO<sub>2</sub> (anatase, BET surface area = 55 m<sup>2</sup>/g) series; between 0.1 and 3.5 wt.% (the wt.% of IrO<sub>2</sub> is converted to micromoles per g of catalyst in the x-axis). The slope of the linear regression of 1.81 is close to the theoretically expected one (2H<sub>2</sub> + IrO<sub>2</sub> → 2H<sub>2</sub>O + Ir). Error bars are 15%.

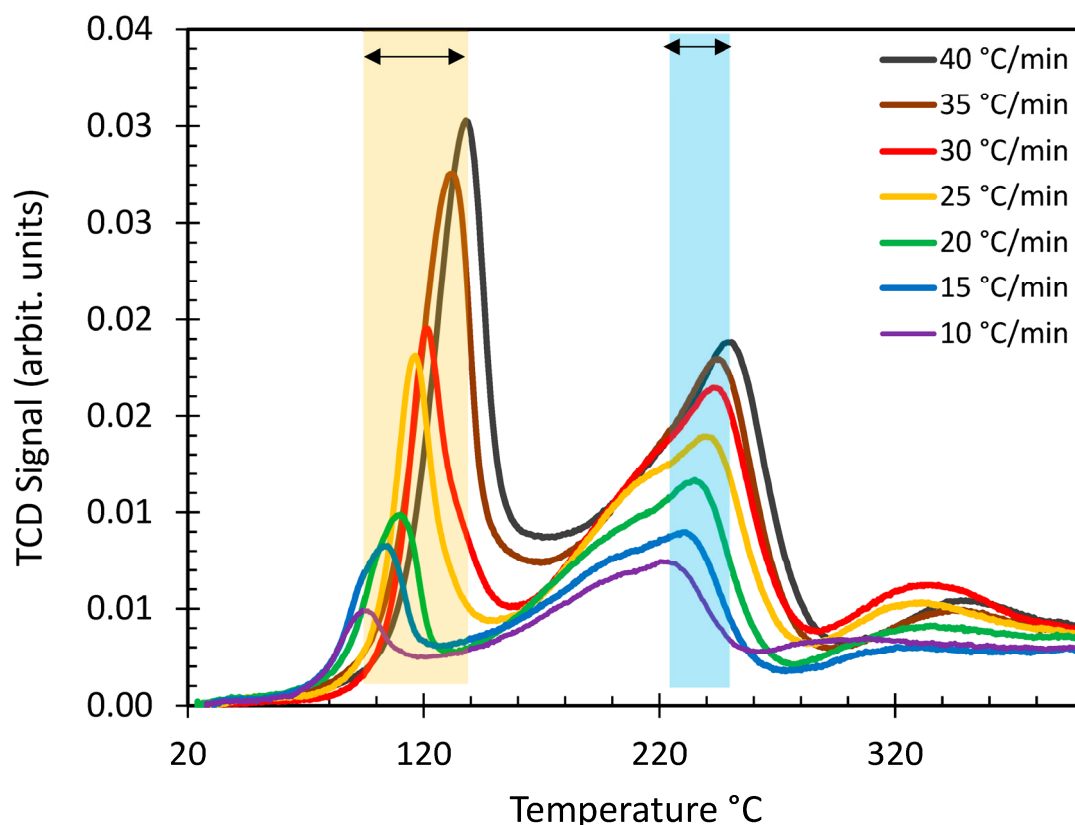


**Figure 2.** TPR patterns of 3.5 wt.% IrO<sub>2</sub>-TiO<sub>2</sub> (anatase, BET surface area = 55 m<sup>2</sup>/g) sample at different ramping rates from 10 to 40 °C/min (a fresh catalyst was put in each run with weight ranging from 58.4 to 61.3 mg). The errors associated with the ramping rates are about 5%.

It was opted to focus on a sample containing a high loading of Ir to minimize errors due to signal to noise ratios. Therefore, the kinetic study of the 3.5 wt.% IrO<sub>2</sub>/TiO<sub>2</sub> TPR pattern was conducted. Figure 2 illustrates the different ramping rates ( $\beta = 10, 15, 20, 25, 30, 35, 40$  °C/min) in H<sub>2</sub>-TPR experiments. TPR data analysis is presented in Table 2. The TPR integrated peak areas are around 6–7 cm<sup>3</sup>/g, and the area increases as the ramp rate increases (see Supporting Information Figure S1 and Figure 2). Note the expected shift to higher temperatures with increasing ramping rates;  $\Delta T_m$  was found to be ca. 40 °C between the slowest and fastest ramping rates used for the first peak and about 25 °C for the second one.

**Table 2.** TPR data analysis of 3.5 wt.% IrO<sub>2</sub>-TiO<sub>2</sub> (anatase, BET = 55 m<sup>2</sup>/g) with variable ramping rates  $\beta$ .

$\beta$ (K/min)	Integrated Peak Area (cm <sup>3</sup> /g) ±0.1	Trapezoid Area (Using end Points as Baseline) ± 0.05	H <sub>2</sub> (mL/g) ± 0.01	H/Ir ±0.2	$T_m$ (°C)		
					1st Peak ±1	2nd Peak ±1	3rd Peak ±1
10	6.83	0.72	0.43	4.23	94	220	309
15	6.82	0.90	0.41	4.23	105	231	330
20	6.50	1.08	0.40	4.02	110	235	335
25	6.31	1.52	0.39	3.91	104	239	331
30	6.48	1.73	0.39	4.01	117	243	333
35	6.28	2.07	0.39	3.89	132	245	343
40	6.00	2.20	0.37	3.71	138	249	348

Two methods were used to model the reduction behavior. First, Kissinger's method was used to calculate the apparent activation energy ( $E_a$ ). Given the corresponding  $\beta$  and  $T_m$  values obtained from TPR, the Kissinger's method was applied to plot  $\ln(\beta/T_m^2)$  against  $1/T_m$  for each set of peaks (Figure 3). The slope equals the apparent activation energy ( $E_a$ ).

over the gas constant ( $R$ ).  $E_a$  values for the reduction of first set of peaks ( $T_m = 94\text{--}138\text{ }^\circ\text{C}$ ) and the reduction of second set of peaks ( $T_m = 220\text{--}249\text{ }^\circ\text{C}$ ) were measured to be 35 and 100 kJ/mol, respectively (Figure 3). These  $E_a$  values imply that the reduction of amorphous iridium oxide (first peak) requires less energy than that of the rutile (crystalline) form (second peak).

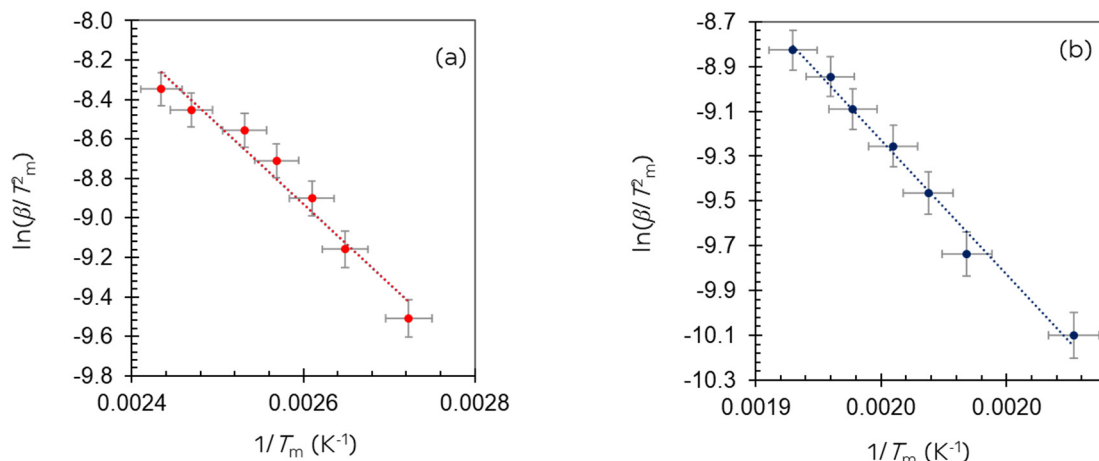


**Figure 3.** Plots of  $\ln(\beta/T_m^2)$  vs.  $1/T_m$  TPR data points collected from TPR of 3.5 wt.%  $\text{IrO}_2/\text{TiO}_2$  (anatase, BET =  $55\text{ m}^2/\text{g}$ ). The linear regression is (a)  $y = -4028.9x + 1.5466$ ,  $R^2 = 0.96$  for the first set peaks, and (b)  $y = -11976x + 14.123$ ,  $R^2 = 0.99$  for the second set peaks.

The second method consisted of applying the different models in Table 2 and testing how they fit with the experimental results. The ramping rate of  $10\text{ }^\circ\text{C}/\text{min}$  ( $\beta = 10$ ) was selected to extract the kinetic parameters using the reduction models; we did not find a noticeable change when the ramping rate was changed (see results of the ramping rate,  $\beta$  was equal to  $40\text{ }^\circ\text{C}/\text{min}$  in the Supporting Material, Figure S2). Figure 4a,b presents the TCD signal against temperature plots in Kelvin for the first and second reduction steps, respectively. The signal was then normalized and plotted as  $\alpha$  (extent of reduction) in which a zero to one scale is for the metal formation with one indicating the total reduction of metal oxides to metal.

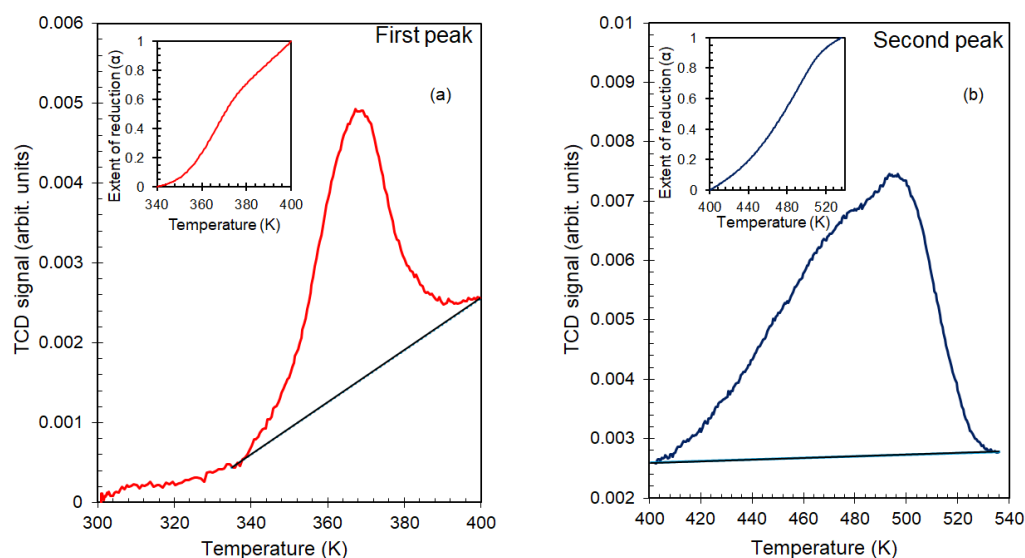


**Figure 4.** Selected TCD signals during TPR of 3.5% wt.%  $\text{IrO}_2/\text{TiO}_2$  (anatase, BET surface area =  $55\text{ m}^2/\text{g}$ ) and their respective  $\alpha$  (extent of reduction, in the insets) for the first (a) and second (b) reduction steps.



Before presenting the fitted results, and because these models may shed light onto the reduction mechanism it is worth discussing the dispersion and crystallite sizes of IrO<sub>2</sub> on the support. We have opted to focus the TEM study on the first peak because its reduction shape (during TPR) is simpler than the second one and because of the low temperature (common to other noble metals) would have marginal contribution from the support. The results are displayed in Figures 5 and 6. As can be seen, there are only negligible differences between the images of the “as prepared” and when reduced up to 120 °C. The mean particles size in both cases is the same (ca. 0.85 nm). However, in general, the particles are brighter after reduction. This is related to their partial transformation into a more metallic state (higher contrast with the support, TiO<sub>2</sub>). The particles are also rounder in shape (less interaction with the support) and have a narrower distribution with a median size slightly larger for the reduced one (0.7 nm for the as-prepared and 0.8–0.9 for the 120 °C reduced ones). Since a non-negligible amount of H<sub>2</sub> is consumed during the first peak (about third of the total amount), the image of Figure 6 contains a non-negligible amount of Ir. Because of the still unchanged particle size, this hydrogen consumption would be related to the removal of oxygen atoms from these clusters making Ir metal.

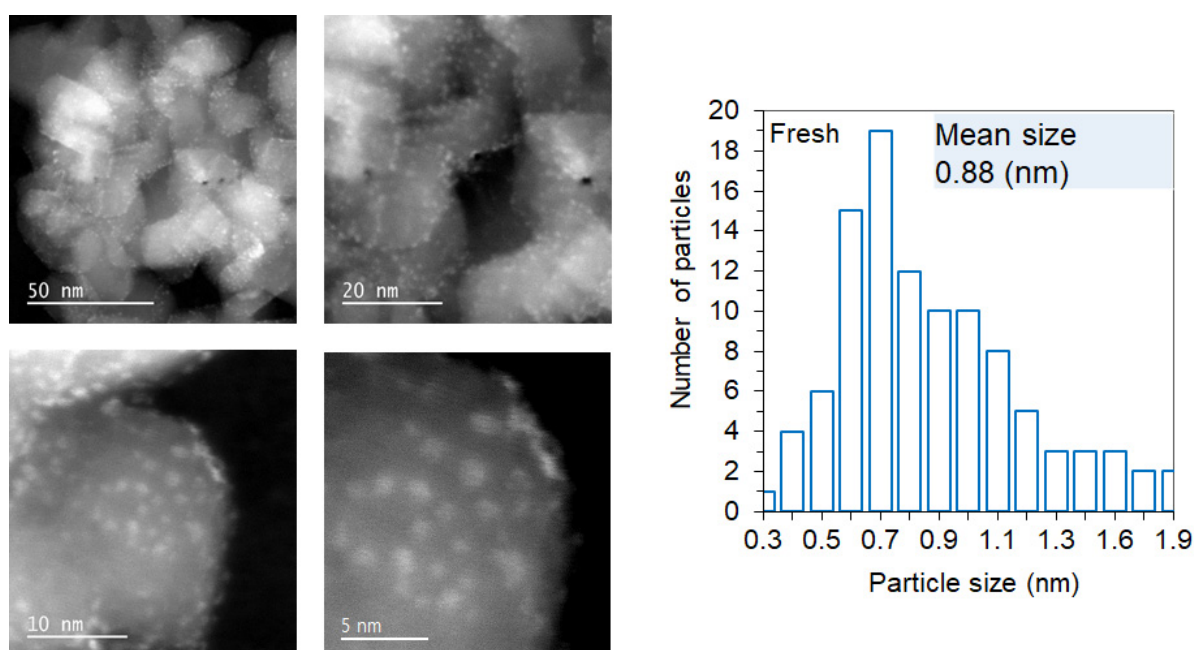


**Figure 5.** TEM images and extracted mean particle size of as-prepared 3.5 wt.% IrO<sub>2</sub>/TiO<sub>2</sub> (anatase, BET surface area = 55 m<sup>2</sup>/g) at different magnifications. Standard errors (0.03 nm).

These changes are not accompanied by changes in the TiO<sub>2</sub> (anatase) phase, as seen before on the same oxide [40], nor with a noticeable change in the weak diffraction of the rutile phase of IrO<sub>2</sub> on top of TiO<sub>2</sub> for the annealed sample and the weak diffraction for the Ir metal for the H<sub>2</sub>-reduced sample (see XRD patterns in Figures S3 and S4, respectively).

Experimental and calculated  $d\alpha/dT$  for the first reduction step is shown in Figure 7. The best fit was exhibited by using  $n$ -order reaction and Sestak-Berggren models (Figure 7a,b). It is important to indicate that the  $n$ -order model mostly considers the reactant concentration [41] without invoking other factors such as diffusion, while the Sestak-Berggren model is largely analytical [42] (for example, it can be reduced to the  $n$ -order model with  $m$  and  $p = 0$ ). It is clear from the shape of the curves that the  $n$ -order model fits the data very well. On the other hand, the deviation of the nucleation and phase boundary models from the data is in line with TEM images and may point out that this region is largely affected by the removal of oxygen atoms and less by atomic re-arrangement. Table 3 presents the kinetic parameters estimated using both models. The calculated  $d\alpha/dT$   $n$ -dimensional nucleation model and phase-boundary controlled models do not appear to be good fitting models

(Figure 7c,d). From the best-fit models, the  $E_a$  is equal to 150 kJ/mol for  $n$ -order reaction and 102 kJ/mol for Sestak-Berggren. While these values are remarkably different from the ones reported using Kissinger's method, they are to be taken together with the prefactor because of the known compensation effect [43] in which a decrease in the activation energy is statistically coupled with a decrease in the prefactor (see the last row in Table 3 as an example). In other words, it is not possible to consider the activation energy alone without considering the prefactor while applying these models.

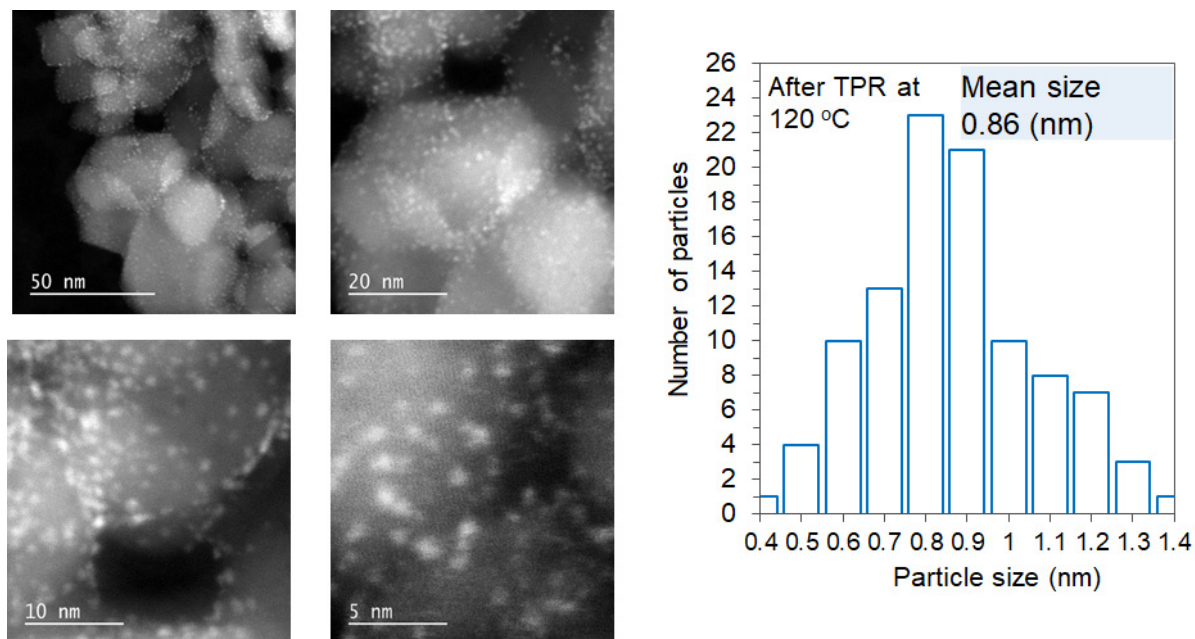


**Figure 6.** TEM images and extracted mean particle size of 3.5 wt.% IrO<sub>2</sub>/TiO<sub>2</sub> (anatase, BET surface area = 55 m<sup>2</sup>/g) that has been reduced during TPR up to 120 °C, at different magnifications. Standard errors (0.02 nm).

The best-fitted  $d\alpha/dT$  models for the second reduction step at 230 °C seem to be the phase boundary-controlled and  $n$ -dimensional nucleation models. A closer inspection indicates that the rise of the peak is best fitted by the phase boundary model, while its fall is best fitted by the  $n$ -dimensional nucleation model. This might have a simple explanation; initially, these small clusters are spread on the support (phase boundary), then during the temperature rise, they are reduced and then nucleate. Shown in Supporting Information, Figure S5 shows the two fitted components of this second region. The first component would be related to the phase boundary effect and the second to nucleation (compare Supporting Information Figure S5 with Figure 8b,c). The qualitative partial agreement of the phase boundary and  $n$ -dimensional nucleation is in line with the expected phase and chemical transformation of IrO<sub>2</sub> to Ir metal. In the modeling, the deviation of  $n$  for the  $n$ -boundary controlled phase to 2.7 (Table 4) is in line with the expected 3D model (theoretically,  $n = 3$  for a contracting sphere model) [44].

It is common for reducible non-noble metal oxides such as Fe<sub>2</sub>O<sub>3</sub> that multiple reduction regions occur [45,46], the first to Fe<sub>3</sub>O<sub>4</sub> (that contains Fe<sup>2+</sup> and Fe<sup>3+</sup>) and FeO (Fe<sup>2+</sup>) while the second to Fe<sup>0</sup>. It is, therefore, possible that after the first reduction peak, the partial reduction of Ir results in a stoichiometrically Ir<sub>2</sub>O<sub>3</sub> (which can be Ir metal on top of IrO<sub>2</sub>) while the second reduces it completely to Ir metal. In this case, the second reduction region would be affected by phase boundary and nucleation together with lattice oxygen removal. However, monitoring subtle changes in the oxidation states of noble metals such as Ir and Pt is not straight forward because of final state effects and the narrow window for the multiple chemical states (for example, the separation between the XPS Ir 4f of Ir metal and that of Ir<sup>4+</sup> is only 1.5 eV which makes it difficult to discern the difference between

multiple oxidation states, final state and ligand effect) [47,48]. Combining the results used by both methods indicates that for quantitative information related to the apparent activation energy, Kissinger's models might be adequate. However, the Kissinger model does not indicate the possible reasons for the reduction of an oxide to a metal. Fitting the data seems to provide further information related to the effect of the support (phase boundary) and the intrinsic properties of IrO<sub>2</sub> to Ir metal (nucleation). It is therefore concluded that both approaches are needed to monitor the reduction of IrO<sub>2</sub> on TiO<sub>2</sub> (anatase) as they are complementary.

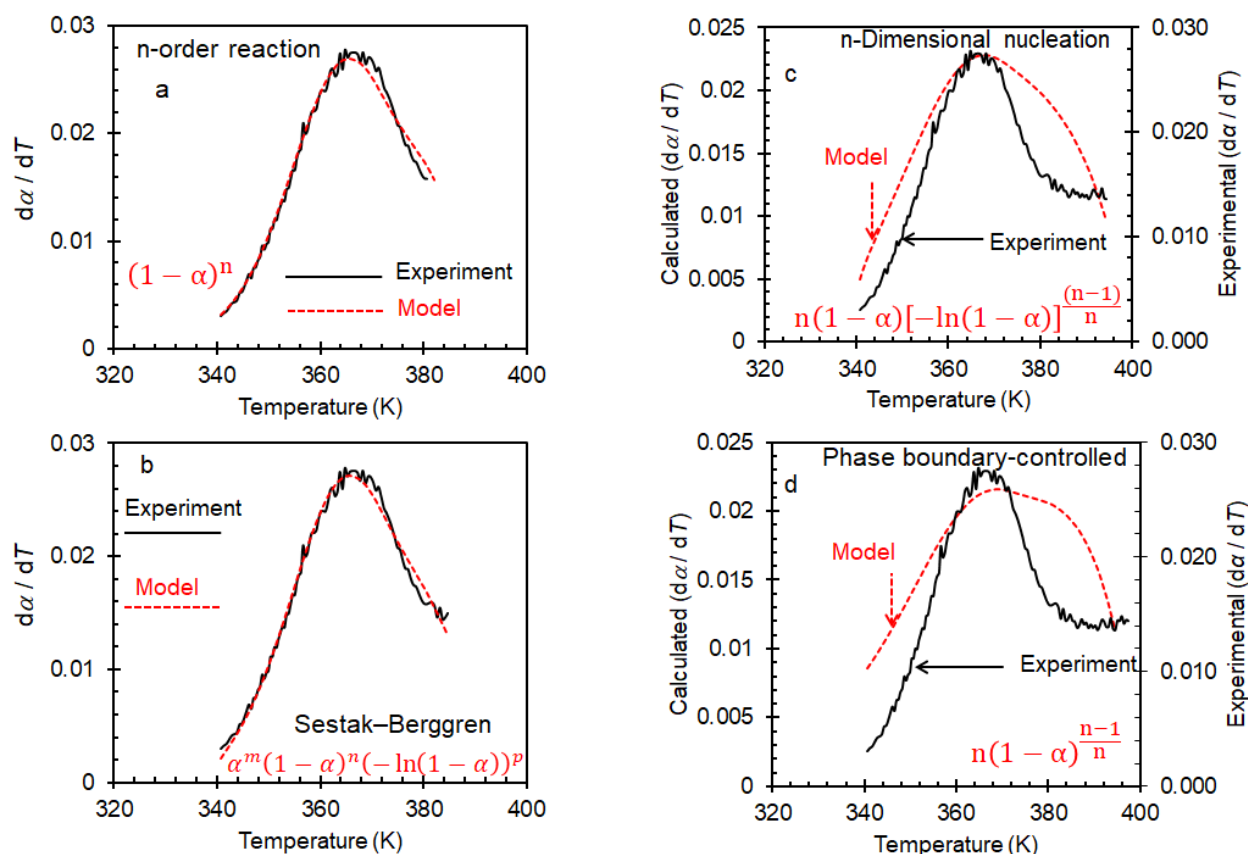


**Figure 7.** Fitted experimental data ( $d\alpha/dT$ ) and calculated ( $d\alpha/dT$ ) using different reduction models (a)  $n$ -order reaction, (b) Sestak–Berggren, (c)  $n$ -dimensional nucleation, (d) phase boundary-controlled) for the first reduction peak during TPR of 3.5% wt.% IrO<sub>2</sub>/TiO<sub>2</sub> (anatase, BET surface area = 55 m<sup>2</sup>/g) with  $\beta = 10$  °C/min.

**Table 3.** Estimated values of the kinetic parameter for the first reduction step during TPR of 3.5% wt.% IrO<sub>2</sub>/TiO<sub>2</sub> (anatase, BET = 55 m<sup>2</sup>/g) with  $\beta = 10$  °C/min. Errors on the activation energy and prefactor taken individually are large, up to 25%. However, taken together, the numbers are exact (as seen in the last row of the table). Errors on  $n$ ,  $m$ , and  $p$  are about 20%.

Kinetic Parameters	$n$ -Order Reaction	Sestak-Berggren
apparent activation energy (kJ/mol)	150	102
pre-exponential factor (s <sup>-1</sup> )	$6.5 \times 10^{19}$	$10^{13}$
$n$	3.2	2.56
$m$	-	0.21
$p$	-	0.06
$\frac{d(\alpha)}{dT} \frac{1}{f(\alpha)}_{T=T_M} = \frac{A}{\beta} \exp\left(\frac{-E_a}{RT_M}\right)$ $T_M = 373$ K	0.384	0.384



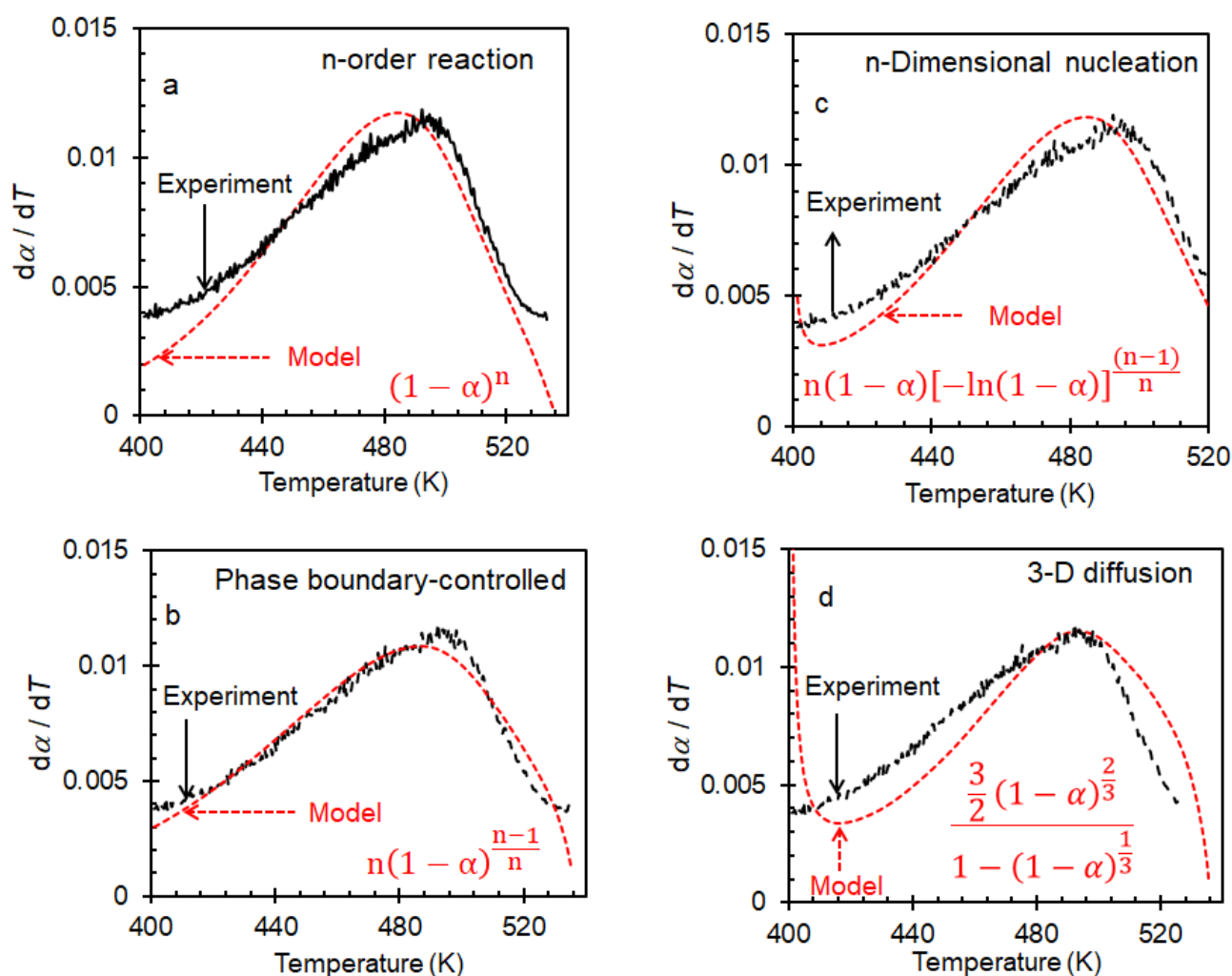


**Figure 8.** Fitted experimental data and calculated ( $d\alpha/dT$ ) using different reduction models (a)  $n$ -order reaction, (b) Phase boundary-controlled, (c)  $n$ -dimensional nucleation, (d) 3-D diffusion) for the second reduction step during TPR of 3.5% wt.%  $\text{IrO}_2/\text{TiO}_2$  (anatase,  $\text{BET} = 55 \text{ m}^2/\text{g}$ ) with  $\beta = 10 \text{ }^\circ\text{C}/\text{min}$ .

**Table 4.** Estimated values of the kinetic parameters using different models for the second reduction reaction during TPR of 3.5% wt.%  $\text{IrO}_2/\text{TiO}_2$  (anatase,  $\text{BET} = 55 \text{ m}^2/\text{g}$ ) with  $\beta = 10 \text{ }^\circ\text{C}/\text{min}$ . Errors on the activation energy and prefactor taken individually are large, up to 25%. However, taken together, the numbers are exact (as seen in the last row of the table). Errors on  $n$  are about 20%.

Kinetic Parameters	$n$ -Order Reaction	$n$ -Dimensional Nucleation	Phase Boundary Controlled
apparent activation energy (kJ/mol)	78	75	36
pre-exponential factor ( $\text{s}^{-1}$ )	$2 \times 10^6$	$7 \times 10^5$	10
$n$	1.4	0.7	2.7
$\frac{d(\alpha)}{dT} \frac{1}{f(\alpha)} \Big _{T=T_M} = \frac{A}{\beta} \exp\left(\frac{-E_a}{RT_M}\right)$ $T_M = 503 \text{ K}$	0.0952	0.0952	0.0952

### 3. Experimental

#### 3.1. Catalyst Preparation

Different wt.% IrO<sub>2</sub> supported on TiO<sub>2</sub> (anatase; BET surface area = 55 m<sup>2</sup>/g) samples were prepared using the wet impregnation method. An Ir<sup>3+</sup> (0.5 mg/mL) stock solution was prepared as follow. The Ir cations were dissolved from dried IrCl<sub>3</sub> (Sigma Aldrich) in deionized water (18.2 MΩ). The solution was stirred overnight until all iridium salt dissolved in water. In parallel, the support TiO<sub>2</sub> (2 g, anatase) was heated at 100 °C for 10 min. Then, the needed amount of Ir<sup>3+</sup> from the stock solution was mixed with TiO<sub>2</sub> and sonicated for 5 min. After that, the mixture was stirred while heated on a hot plate covered with Al foil at 110 °C for about 8 h until the solution has evaporated. The formed paste was spread on a ceramic crucible and calcined at 400 °C (at a ramping rate of 2 °C min<sup>-1</sup>) in a muffle furnace for 5 h under static air. During this process Ir<sup>3+</sup> cations are oxidized to Ir<sup>4+</sup> cations [49].



#### 3.2. Temperature Programmed Reduction (TPR)

H<sub>2</sub>-TPR experiments were conducted in a quartz tube reactor coupled to a thermal conductivity detector (TCD) (AutoChem 2920, Micrometrics). TPR was calibrated using four samples of Ag<sub>2</sub>O (26, 32, 59, and 90 mg). The peak area (*y*-axis) under the TPR curve was linearly proportional to the calculated hydrogen volume (mL) (*x*-axis), resulting in the equation  $y = 2.50x - 4.10$ . For each calibration sample, TPR pattern shows one distinct peak and the stoichiometric ratio between molecular hydrogen and silver metal was found to be equal one. From this calibration we estimated the errors in extracting the quantity needed to reduce the oxide from one run to the other to be about 5%. Catalytic samples of 0.1, 0.3, 0.5, 1.0, 2.0, 2.5, 3.0, and 3.5 wt.% IrO<sub>2</sub>-TiO<sub>2</sub> (~60 mg) were placed on a fritted glass-bed inside the reactor. The samples were then purged with Ar for at least 5 min (50 mL/min), and 10% H<sub>2</sub>-Ar (50 mL/min) was used as the reducing gas. The temperature range of TPR experiments was from room temperature to 400 °C. The percentage concentration of H<sub>2</sub> was obtained from the calibrated TCD signal. The TCD signal against temperature plot (TPR pattern) is generated by AutoChem program during the reduction reaction. The area under the curve corresponds to the amount of hydrogen consumed (cm<sup>3</sup>/g). The total consumption of H<sub>2</sub> was calculated by solving for number of moles in the ideal gas law using the volume of H<sub>2</sub> consumption obtained from AutoChem program integration and under standard pressure and temperature conditions. Trapezoid area calculations using OriginLab were performed.

#### 3.3. Kinetic Study

A method for calculating the apparent activation energy of a solid-state reaction by using differential thermal analysis was early on proposed by Kissinger [12]. This method has been used in the literature to investigate the kinetics of solid-state reactions, including the reduction of metal oxides [13].

The gas-solid reaction rate under differential conditions is described as follows:

$$\text{rate} = \frac{d[\alpha]}{dt} = k(T)f(\alpha) \quad (3)$$

where  $\alpha$  is the degree of conversion of a solid reactant ( $\alpha = \frac{n_t}{n_{total}}$ ) where  $n_t$  is moles of hydrogen consumed at time  $t$  (min) and  $n_{total}$  is represents the total moles of hydrogen consumed.

For the complete reduction of the oxide,  $f(\alpha)$  is a function of reduction models and  $k(T)$  is the rate constant (in reciprocal time) of the Arrhenius equation:

$$k(T) = A \exp\left(\frac{-E_a}{RT}\right) \quad (4)$$

where  $A$  is the pre-exponential factor (reciprocal time),  $E_a$  is the activation energy (joules/mole),  $R$  is the gas constant, and  $T$  is the temperature in Kelvin.

In TPR experiments, the heating rate (K/min) or ramping rate  $\beta$  is equal to  $\frac{dT}{dt}$ ; therefore, by substituting the ramp rate into Equation (1) and combining it with Equation (2), the gas-solid reaction rate equation is written as follows:

$$\frac{d(\alpha)}{dT} = \frac{A}{\beta} \exp\left(\frac{-E_a}{RT}\right) f(\alpha) \quad (5)$$

In this work, two approaches were applied to investigate the kinetics of the 3.5 wt.% IrO<sub>2</sub>/TiO<sub>2</sub> (anatase) catalyst. First, Kissinger's derived equation was used to determine the apparent activation energy from TPR patterns obtained at different ramp rates. The equation is derived as follows:

$$\begin{aligned} \frac{d}{dT} \left( \frac{d\alpha}{dT} \right)_{T=T_m} &= \frac{d}{dT} \left( \frac{A}{\beta} \exp\left(-\frac{E_a}{RT}\right) f(\alpha) \right)_{T=T_m} = 0 \\ \left( \frac{A}{\beta} \frac{E_a}{RT^2} \exp\left(-\frac{E_a}{RT}\right) f(\alpha) + \frac{A}{\beta} \exp\left(-\frac{E_a}{RT}\right) \frac{df(\alpha)}{d\alpha} \frac{d\alpha}{dT} \right)_{T=T_m} &= 0 \\ \left( \frac{d\alpha}{dT} \left( \frac{E_a}{RT^2} + \frac{A}{\beta} \exp\left(-\frac{E_a}{RT}\right) \frac{df(\alpha)}{d\alpha} \right) \right)_{T=T_m} &= 0 \\ \left( \frac{E_a}{RT_m^2} + \frac{A}{\beta} \exp\left(-\frac{E_a}{RT_m}\right) \frac{df(\alpha)}{d\alpha} \right) &= 0 \\ \frac{E_a}{RT_m^2} = \frac{A}{\beta} \exp\left(-\frac{E_a}{RT_m}\right) \left( -\frac{df(\alpha)}{d\alpha} \right)_{T=T_m} \\ \ln\left(\frac{\beta}{T_m^2}\right) + \ln\left(\frac{E_a}{RA}\right) &= -\frac{E_a}{RT_m} + \ln\left(-\frac{df(\alpha)}{d\alpha}\right)_{T=T_m} \end{aligned} \quad (6)$$

$T_m$  is the maximum temperature in a TPR pattern, which is commonly taken as the summit point of a peak. Therefore plotting  $\ln\left(\frac{\beta}{T_m^2}\right)$  versus  $\frac{1}{T_m}$  gives a straight line in which the slope is equal to  $\frac{-E_a}{R}$ .

The second method consisted of extracting the kinetics parameters (apparent activation energy, pre-exponential factor, by a reduction model). These were determined by plotting the calculated  $\frac{d(\alpha)}{dT}$  and fitting it into experimental  $\frac{d(\alpha)}{dT}$  using solver in Microsoft Excel. The best model fit is achieved by varying those three variables ( $E_a$ ,  $A$ , and  $f(\alpha)$ ) in Equation (3). The extent of reduction ( $\alpha$ ) was produced for each peak in TPR patterns. Table 5 contains typical reduction models used in solid-gas reactions.

**Table 5.** Common reduction functions reported in the literature.

Reaction Model	$f(\alpha)$
$n$ -dimensional nucleation-Avrami-Erofeev	$n(1-\alpha)[- \ln(1-\alpha)]^{\frac{(n-1)}{n}}$
$n$ -order reaction	$(1-\alpha)^n$
Phase boundary-controlled	$n(1-\alpha)^{\frac{n-1}{n}}$
1-D diffusion	$\frac{1}{2}\alpha^{-1}$
2-D diffusion	$\frac{-1}{\ln(1-\alpha)}$
3-D diffusion	$\frac{3}{2}(1-\alpha)^{\frac{2}{3}}$
Sestak-Berggren	$\frac{1-(1-\alpha)^{\frac{1}{3}}}{1-(1-\alpha)^{\frac{1}{3}}}$
	$\alpha^m(1-\alpha)^n(-\ln(1-\alpha))^p$

#### 4. Conclusions

H<sub>2</sub>-TPR experiments of IrO<sub>2</sub>/TiO<sub>2</sub> (anatase) were conducted with a focus on two regions where IrO<sub>2</sub> is reduced (in part) to Ir metal at ca. 100 and totally at 230 °C. Based on

TPR and TEM results, the first peak is due to the partial reduction of small clusters (less than 1 nm in size) of IrO<sub>2</sub> to Ir metal, and the second one is due to the reduction of the formed crystalline phase (rutile), during TPR, to the metal. Two methods for calculating kinetic parameters were considered. First, using TPR patterns, different applied ramp rates ( $\beta$  changed from 10 to 40 K/min) of a 3.5 wt.% IrO<sub>2</sub>/TiO<sub>2</sub> were conducted for the use of Kissinger's method. The apparent activation energy values for the first and second reduction reactions were found to be ca. 35 and 100 kJ/mol, respectively. The second method involved separating TPR patterns of the 3.5 wt.% IrO<sub>2</sub>/TiO<sub>2</sub> sample at a constant ramping rate ( $\beta = 10$  and 40 K/min) modeled using different gas-solid reduction functions. The best model-fit between experimental and calculated  $d\alpha/dT$  for the first reduction step is an  $n$ -order reaction, while no complete agreement with any model was found for the second peak. However, it seems that the reduction in the second region is best explained by a combination of two models (phase boundary and nucleation). It is clear from this work that the nature of the interaction of IrO<sub>2</sub> with the support dictates its reduction kinetics. Results indicate that multiple peaks for reduction found for noble metals dispersed on an oxide originate from reconstructions of the clusters in addition to successive reduction steps. Further refinement of the models with a focus on the  $n$ -boundary and nucleation ones may provide a more complete picture. This is particularly important because of the possible coupling with the reduction of the support, TiO<sub>2</sub>, at temperatures above 300 °C, which is neglected for the sake of simplicity in this study.

**Supplementary Materials:** The following supporting information can be downloaded at: <https://www.mdpi.com/article/10.3390/inorganics11020066/s1>, Figure S1: Raw data for the TPR of 3.5% wt. % IrO<sub>2</sub>/TiO<sub>2</sub>; Figure S2: Fitted experimental data and calculated ( $d\alpha/dT$ ) using different reduction models; Figure S3: XRD of 3.5 wt.% IrO<sub>2</sub>/TiO<sub>2</sub> annealed at 400 °C and 600 °C; Figure S4: XRD of 3.5 wt.% IrO<sub>2</sub>/TiO<sub>2</sub> (anatase, BET = 55 m<sup>2</sup>/g) reduced at 400 °C (black dots) and 500 °C (red dots); Figure S5: Deconvoluted experimental data for the second reduction step during TPR.

**Author Contributions:** Conceptualization, H.I.; Investigation, S.B., M.A. and M.A.N.; Writing—original draft, S.B.; Writing—review & editing, H.I.; Supervision, M.A. and H.I. All authors have read and agreed to the published version of the manuscript.

**Funding:** This research received no external funding.

**Data Availability Statement:** Data can be requested directly from the corresponding author, H.I.

**Conflicts of Interest:** The authors declare no conflict of interest.

## References

1. van Deelen, T.W.; Mejía, C.H.; de Jong, K.P. Control of metal-support interactions in heterogeneous catalysts to enhance activity and selectivity. *Nat. Catal.* **2019**, *2*, 955–970. [[CrossRef](#)]
2. Liu, L.; Corma, A. Metal Catalysts for Heterogeneous Catalysis: From Single Atoms to Nanoclusters and Nanoparticles. *Chem. Rev.* **2018**, *118*, 4981–5079. [[CrossRef](#)] [[PubMed](#)]
3. Moulijn, J.A.; van Leeuwen, P.W.N.M.; van Santen, R.A. (Eds.) An Integrated Approach to Homogeneous, Heterogeneous and Industrial Catalysis, Chapter 11, Temperature Programmed Reduction and Sulphiding. *Stud. Surf. Sci. Catal.* **1993**, *79*, 401–417.
4. Hurst, N.W.; Gentry, S.J.; Jones, A.; McNicol, B.D. Temperature Programmed Reduction. *Catal. Rev. Sci. Eng.* **1982**, *24*, 233–309. [[CrossRef](#)]
5. Lou, Y.; Xu, J.; Zhang, Y.; Pana, C.; Dong, Y.; Zhu, Y. Metal-Support Interaction for Heterogeneous Catalysis: From Nanoparticles to Single Atoms. *Mat. Today Nano* **2020**, *12*, 100093. [[CrossRef](#)]
6. Abdel Halim, K.S.; El-Geassy, A.A.; Ramadan, M.; Nasr, M.I.; Hussein, A.; Fathy, N.; Alghamdi, A.S. Reduction Behavior and Characteristics of Metal Oxides in the Nanoscale. *Metals* **2022**, *12*, 2182. [[CrossRef](#)]
7. Diagne, C.; Idriss, H.; Pearson, K.; Gómez-García, M.A.; Kiennemann, A. Efficient Hydrogen Production by Ethanol Reforming over Rh Catalysts. Effect of Addition of Zr on CeO<sub>2</sub> for the Oxidation of CO to CO<sub>2</sub>. *Comptes Rendus Chim.* **2004**, *7*, 617–622. [[CrossRef](#)]
8. Al-Shankiti, I.; Al-Otaibi, F.M.; Al-Salik, Y.; Idriss, H. Solar Thermal Hydrogen Production over CeO<sub>2</sub> Based Materials. *Top. Catal.* **2013**, *56*, 1129–1138. [[CrossRef](#)]
9. Lokteva, E.S.; Golubina, E.V. Metal-Support Interactions in the Design of Heterogeneous Catalysts for Redox Processes. *Pure Appl. Chem.* **2019**, *91*, 609–631.

10. Wang, Y.; Arandiyani, H.; Bartlett, S.A.; Trunschke, A.; Sunf, H.; Scott, J.; Lee, A.F.; Wilson, K.; Maschmeyer, T.; Schlögl, R.; et al. Inducing Synergy in Bimetallic RhNi Catalysts for CO<sub>2</sub> Methanation by Galvanic Replacement. *Appl. Catal. B Environ.* **2020**, *277*, 119029. [[CrossRef](#)]
11. Fedorov, A.V.; Kukushkin, R.G.; Yeletsky, P.M.; Bulavchenko, O.A.; Chesalov, Y.A.; Yakovlev, V.A. Temperature-Programmed Reduction of Model CuO, NiO and Mixed CuO-NiO Catalysts with Hydrogen. *J. Alloy. Comp.* **2020**, *844*, 156135. [[CrossRef](#)]
12. Kissinger, H.E. Reaction Kinetics in Differential Thermal Analysis. *Anal. Chem.* **1957**, *29*, 1702–1706. [[CrossRef](#)]
13. Adnađević, B.J.; Mentus, S. The Kinetic Study of Temperature-Programmed Reduction of Nickel Oxide in Hydrogen Atmosphere. *Chem. Eng. Sci.* **2008**, *63*, 567–575.
14. Ghaani, M.R.; Catti, M. Investigation on the Kinetic Mechanism of the Reduction of Fe<sub>2</sub>O<sub>3</sub>/CoO-Decorated carbon Xerogels: A Non-Isothermal Study. *J. Solid State Chem.* **2019**, *277*, 368–375. [[CrossRef](#)]
15. Samoila, P.; Boutzeloit, M.; Especel, C.; Epron, F.; Marécot, O. Relationship Between the Structural Properties of Supported Bimetallic Pt–Rh Catalysts and their Performances for Methylcyclopentane ring opening. *J. Catal.* **2010**, *276*, 237–248. [[CrossRef](#)]
16. Srisin Eaimsumang, S.; Prataksanon, P.; Pongstabodee, S.; Luengnaruemitchai, A. Effect of Acid on the Crystalline Phase of TiO<sub>2</sub> Prepared by Hydrothermal Treatment and its Application in the Oxidative Steam Reforming of Methanol. *Res. Chem. Intermed.* **2020**, *46*, 1235–1254. [[CrossRef](#)]
17. Kammert, J.; Moon, J.; Wu, Z. A review of the Interactions Between Ceria and H<sub>2</sub> and the Applications to Selective Hydrogenation of Alkynes. *Chin. J. Catal.* **2020**, *41*, 901–914. [[CrossRef](#)]
18. Al-Taweel, S.; Nadeem, M.A.; Idriss, H. A study of Ce<sub>x</sub>Fe<sub>1-x</sub>O<sub>2</sub> as a reducible oxide for the thermal hydrogen production from water. *Energy Technol.* **2021**, *10*, 2100491. [[CrossRef](#)]
19. Boodts, J.C.F.; Trsdstti, S. Hydrogen Evolution on Iridium Oxide Cathodes. *J. Appl. Electrochem.* **1988**, *19*, 255–262. [[CrossRef](#)]
20. Gao, J.; Liu, Y.; Liu, B.; Huang, K.W. Progress of Heterogeneous Iridium-Based Water Oxidation Catalysts. *ACS Nano* **2022**, *16*, 17761–17777. [[CrossRef](#)]
21. Hunt, L.B. A History of Iridium Overcoming the Difficulties Of Melting and Fabrication. *Platin. Met. Rev.* **1987**, *31*, 32–41.
22. Jin, R.; Peng, M.; Li, A.; Deng, Y.; Jia, Z.; Huang, F.; Ling, Y.; Yang, F.; Fu, H.; Xie, J.; et al. Low Temperature Oxidation of Ethane to Oxygenates by Oxygen over Iridium-Cluster Catalysts. *J. Am. Chem. Soc.* **2019**, *141*, 18921–18925. [[CrossRef](#)] [[PubMed](#)]
23. Liu, F.; Pak, E.B.; Singh, B.; Jensen, C.M.; Goldman, A.S. Dehydrogenation of n-Alkanes Catalyzed by Iridium “Pincer” Complexes: Regioselective Formation of r-Olefins. *J. Am. Chem. Soc.* **1999**, *121*, 4086–4087. [[CrossRef](#)]
24. Liang, Z.; Li, T.; Kim, M.; Asthagiri, A.; Weaver, J.F. Low-temperature Activation of Methane on the IrO<sub>2</sub>(110) Surface. *Science* **2017**, *356*, 299–303. [[CrossRef](#)] [[PubMed](#)]
25. Seth, J.; Dubey, P.; Chaudhari, V.R.; Prasad, B.L.V. Preparation of Metal Oxide Supported Catalysts and Their Utilization for Understanding the Effect of a Support on the Catalytic Activity. *New J. Chem.* **2018**, *42*, 402–410. [[CrossRef](#)]
26. Czioska, S.; Boubnov, A.; Escalera-López, D.; Geppert, J.; Zagalskaya, A.; Röse, P.; Saraçi, E.; Alexandrov, V.; Krewer, U.; Cherevko, S.; et al. Increased Ir–Ir Interaction in Iridium Oxide during the Oxygen Evolution Reaction at High Potentials Probed by Operando Spectroscopy. *ACS Catal.* **2021**, *11*, 10043–10057. [[CrossRef](#)]
27. Alrushaid, M.; Wahab, K.A.; Nadeem, M.A.; Idriss, H. Extracting Turn Over Frequencies of Electron Transfer in Heterogeneous Catalysis. A study of IrO<sub>2</sub>-TiO<sub>2</sub> Anatase for Water Oxidation Using Ce<sup>4+</sup> Cations. *Catalysts* **2021**, *11*, 1030. [[CrossRef](#)]
28. Bashir, S.; Idriss, H. Temperature Programmed Desorption of ethanol Over TiO<sub>2</sub> and M/TiO<sub>2</sub> (M = Au, Pd and Au-Pd) Catalysts: Dehydration Versus de-Carbonylation Pathways. *Top. Catal.* **2018**, *61*, 487–498. [[CrossRef](#)]
29. Bashir, S.; Idriss, H. Mechanistic Study of the Role of Au, Pd and Au-Pd on the Surface Photo-Reactions of Ethanol Over TiO<sub>2</sub>. *Catal. Sci. Technol.* **2017**, *7*, 5301–5320. [[CrossRef](#)]
30. King, R.; Idriss, H. Acetone Reactions Over the Surfaces of Polycrystalline UO<sub>2</sub>. A Kinetic and Spectroscopic Study. *Langmuir* **2009**, *25*, 4543–4555. [[CrossRef](#)]
31. Bashir, S.; Idriss, H. The Reaction of Hydrogen Peroxide and Propylene to Propylene Oxide on the Surface of CeO<sub>2</sub>: An in situ FTIR Spectroscopy and Temperature Programmed Desorption Study. *J. Chem. Phys.* **2020**, *152*, 044712. [[CrossRef](#)]
32. Wilson, J.R.; Idriss, H. Reactions of Ammonia on Stoichiometric and Reduced TiO<sub>2</sub>(001) Single Crystal Surfaces. *Langmuir* **2004**, *20*, 10956–11096. [[CrossRef](#)]
33. Millican, S.L.; Androshchuk, I.; Tran, J.T.; Trottier, R.M.; Bayon, A.; Al Salik, Y.; Idriss, H.; Musgrave, C.B.; Weimer, A.W. Oxidation Kinetics of Hercynite Alloys for Solar Thermochemical Fuel Production. *Chem. Eng. J.* **2020**, *401*, 126015. [[CrossRef](#)]
34. Yarar, M.; Bouziani, A.; Uner, D. Pd as a Reduction Promoter for TiO<sub>2</sub>: Oxygen and Hydrogen Transport at 2D and 3D Pd Interfaces with TiO<sub>2</sub> Monitored by TPR, Operando 1H NMR and CO Oxidation Studies. *Catal. Comm.* **2023**, *174*, 106580. [[CrossRef](#)]
35. Hernández-Cristoibal, O.; Díaz, G.; Gómez-Cortés, A. Effect of the Reduction Temperature on the Activity and Selectivity of Titania-Supported Iridium Nanoparticles for Methylcyclopentane Reaction. *Ind. Eng. Chem. Res.* **2014**, *53*, 10097–10104. [[CrossRef](#)]
36. Yu, H.; Wada, K.; Fukutake, T.; Feng, Q.; Uemura, S.; Isoda, K.; Hirai, T.; Iwamoto, S. Effect of Phosphorus-Modification of Titania Supports on the Iridium Catalyzed Synthesis of Benzimidazoles. *Catal. Today* **2021**, *375*, 410–417. [[CrossRef](#)]
37. Rice, R.W.; Chien, C.C. Simulation of Supported Iridium Catalyst Sintering and Redispersion. *J. Catal.* **1987**, *103*, 140–150. [[CrossRef](#)]



38. Zhang, Y.; Zhang, Z.; Yang, X.; Wang, R.; Duan, H.; Shen, Z.; Li, L.; Su, Y.; Yang, R.; Zhang, Y.; et al. Tuning Selectivity of CO<sub>2</sub> Hydrogenation by Modulating the Strong Metal–Support Interaction Over Ir/TiO<sub>2</sub> catalysts. *Green Chem.* **2020**, *22*, 6855–6861. [[CrossRef](#)]
39. Pfeifer, V.; Jones, T.E.; Vélez, J.J.V.; Massué, C.; Arrigo, R.; Teschner, D.; Girgsdies, F.; Scherzer, M.; Greiner, M.T.; Allan, J. The Electronic Structure of Iridium and its Oxides. *Surf. Interface Anal.* **2016**, *48*, 261–273. [[CrossRef](#)]
40. Bashir, S.; Wahab, A.K.; Idriss, H. Synergism and Photocatalytic Water Splitting to Hydrogen Over Pt/TiO<sub>2</sub> Catalysts: Effect Particle Size. *Catal. Today* **2015**, *240*, 242–247. [[CrossRef](#)]
41. Gamisch, B.; Huber, L.; Gaderer, M.; Dawoud, B. On the Kinetic Mechanisms of the Reduction and Oxidation Reactions of Iron Oxide/Iron Pellets for a Hydrogen Storage Process. *Energies* **2022**, *15*, 8322. [[CrossRef](#)]
42. Munteanu, G.; Segal, E. Sestak–Berggren Function in Temperature-Programmed Reduction. *J. Therm. Anal. Calorim.* **2010**, *101*, 89–95. [[CrossRef](#)]
43. Bond, G.C.; Keane, M.A.; Kral, H.; Lercher, J.A. Compensation Phenomena in Heterogeneous Catalysis: General Principles and a Possible Explanation. *Catal. Rev. Sci. Eng.* **2010**, *42*, 323–383. [[CrossRef](#)]
44. Lup, A.N.K.; Abnisa, F.; Daud, W.M.A.; Aroua, M.K. Temperature-Programmed Reduction of Silver(I) Oxide Using a Titania-Supported Silver Catalyst Under a H<sub>2</sub> Atmosphere. *J. Chin. Chem. Soc.* **2019**, *66*, 1443–1455. [[CrossRef](#)]
45. Manchili, S.K.; Wendel, J.; Hryha, E.; Nyborg, L. Analysis of Iron Oxide Reduction Kinetics in the Nanometric Scale Using Hydrogen. *Nanomaterials* **2020**, *10*, 1276. [[CrossRef](#)]
46. Musolino, M.G.; Busacca, C.; Mauriello, F.F.; Rosario Pietropaolo, R. Aliphatic Carbonyl Reduction Promoted by Palladium Catalysts Under Mild Conditions. *Appl. Catal. A Gen.* **2010**, *379*, 77–86. [[CrossRef](#)]
47. Wei, G.; Wang, Y.; Huang, C.; Gao, Q.; Wang, Z.; Xu, L. The stability of MEA in SPE Water Electrolysis for Hydrogen Production. *Int. J. Hydrog. Energy* **2010**, *35*, 3951–3957. [[CrossRef](#)]
48. Hara, M.; Asami, K.; Hashimoto, K.; Masumoto, T. An X-ray Photoelectron Spectroscopic Study of Electrocatalytic Activity of Platinum Group Metals for Chlorine evolution. *Electrochem. Acta* **1983**, *28*, 1073–1081. [[CrossRef](#)]
49. Amaya, S.A.D. Electrochemical Evaluation of Oxygen Evolution Reaction Electrocatalysts: The Case of Ultraporous Iridium Oxide and Iridium-Based Mixed Oxide Materials. Ph.D. Thesis, Institut Polytechnique de Paris, Paris, France, 2021.

**Disclaimer/Publisher’s Note:** The statements, opinions and data contained in all publications are solely those of the individual author(s) and contributor(s) and not of MDPI and/or the editor(s). MDPI and/or the editor(s) disclaim responsibility for any injury to people or property resulting from any ideas, methods, instructions or products referred to in the content.